Master's thesis

Hyperspectral imaging of tissues

Eszter Gábriel

Supervisor: Václav Hanus
HUN-REN Wigner Research Centre for Physics

Supervisor: Péter Dombi
HUN-REN Wigner Research Centre for Physics

Consultant: Csilla Pesznyák
National Institute of Oncology

Budapest University of Technology and Economics
2026

MŰEGYETEM 1782

Szakdolgozat-választás

A hallgató neve: Gábriel Eszter	specializációja: Orvosi fizika MSc
A záróvizsgát szervező tanszék neve: NTI	

A témavezető neve: Václav Hanus PhD - munkahelye: MTA Központi Fizikai Kutatóintézet (KFKI) - beosztása: tudományos munkatárs - email címe: hanus.vaclav@wigner.hun-ren.hu	A konzulens neve: Dr. Pesznyák Csilla - tanszéke: NTI - beosztása: egyetemi docens - email címe: pesznyak@reak.bme.hu

A kidolgozandó feladat címe: A szövetek hiperspektrális képalkotása

A téma rövid leírása, a megoldandó legfontosabb feladatok felsorolása:

Hyperspectral imaging attains increasing interest in many areas of photonic industry from satellite imagery to health care [1,2] and agriculture [3]. Hyperspectral imaging, that stands for a complete spectral resolution of a photograph, gives an extended view of the world around us, otherwise perceived only through red-green-blue composite imagery. The availability of well-defined white light sources, robust spectrometer technology, and fast image processing methods bring the hyperspectral imaging capabilities closer to impactful applications. One of the intriguing applications is studying metabolic processes in living tissues. Spatially resolved spectral information of the tissues gives a detailed insight into the state of the tissue as it provides information about healthiness of the tissue and uncovers starting pathologies of the tissues.

Goals:

The goal of the master thesis is to perform a case study of the living tissues of a plant using hyperspectral imaging. For this, the applicant will construct an imaging chamber, where hyperspectral images will be taken. The applicant will use a white-light fiber laser source for well-defined illumination conditions and construct a lens-based imaging system to capture a two-dimensional spectrally resolved image. The 2D collection of the spectral information will be achieved by scanning an input of an optical fiber over the image plane of the imaging system. The spectrum acquisition is then ensured by the connection of the optical fiber to a spectrometer.

The applicant will design the parameters of the imaging and acquisition system as well as a platform for processing the images. The evolution and presence of a pathology in the tissue will be monitored and described.

Training:

The master candidate would learn operating laser technology and will get familiar with fundamental techniques related to optics, image acquisition and processing. The candidate would have the opportunity to develop and realize own experiments to pursuit the set-up goals.

A záróvizsga kijelölt tételei:

Dátum:

Hallgató aláírása:	Témavezető aláírása*:	Tanszéki konzulens aláírása:	A témakiírását jóváhagyom (tanszékvezető aláírása):

*A témavezető jelen feladatkiírás aláírásával tudomásul veszi, hogy a BME TVSZ 145. és 146.§ alapján az egyetem a képzési célok megvalósulása érdekében a szakdolgozatok, illetve diplomamunkák nyilvánosságát tartja elsődlegesnek. A hozzáférés korlátozása csak kivételes esetben, a dékán előzetes hozzájárulásával lehetséges.

Declaration of Originality

Undersigned **Eszter Gábriel**, physics MSc student of the Budapest University of Technology and Economics, declare that I wrote this thesis without the use of any unauthorized assistance, under the guidance of my supervisor. I have cited every source I used. For any part that I have borrowed verbatim, or paraphrased while preserving its original meaning, I have marked its source of origin.
Budapest, May 2026

Gábriel Eszter

.....

Eszter Gábriel

Identicality of digital and printed versions

Undersigned **Eszter Gábriel** physics MSc student of the Budapest University of Technology and Economics, declare that the digital and printed copies of the thesis are identical in all respects.
Budapest, May 2026

Gábriel Eszter

Eszter Gábriel

Introduction

Hyperspectral imaging (HSI) is an emerging tool used in fundamental research and diverse fields like food quality control, environmental monitoring, and medicine. Its strength lies in combining spatial and spectral information: each pixel is spectrally resolved with hundreds of wavelength channels to construct a three-dimensional data cube [1]. HSI exploits characteristic spectral fingerprints [2] generated by light scattering and absorption within a sample.

While the initial objective of this project was to monitor pathologies in plant tissues, the scope was shifted to zebrafish embryos to evaluate the system's potential on a highly relevant vertebrate model for biomedical research. The broader motivation for this research is to investigate whether HSI can serve as a non-invasive tool to distinguish between irradiated and control zebrafish embryos. If successful, this approach would provide a significant advantage in radiobiology by enabling the identification of spectral markers and radiation-induced tissue effects without altering the samples. As a foundational step, this work establishes the imaging methodology using only control specimens.

To optimize acquisition, a line-scanning configuration was chosen over 3D point-scanning. Unlike point-scanning's slow mechanical translation, line-scanning uses a slit to simultaneously capture an entire spatial row and its spectrum. This drastically reduces acquisition time, which is critical to prevent tissue dehydration.

With this architecture in mind, the primary task of this thesis was to design, construct, calibrate and test the hyperspectral system from the ground up. The development began with a macro-scale camera to validate the fundamental optical pathway, grating dispersion, and software controls. Once this baseline setup proved effective, it was re- engineered into a vertical microscopic system capable of resolving the fine features of ≈ 3 mm zebrafish embryos. For efficient data acquisition, a dedicated program and graphical user interface were developed to automate the camera and servo motor. The optomechanical setup was precisely aligned and calibrated using filters and a neon lamp, allowing the instrument to achieve a magnification of 2.42, a wavelength resolution of 2.4 nm, and a spatial resolution of 8.3 µm across a 300 nm visible spectral range. Finally, it was tested with colored reference samples. The system was then applied to identify the spectral fingerprints of zebrafish embryos using both transmissive and refractive illumination, analyzing the data with the Spectral Angle Mapper (SAM) algorithm.

Ultimately, this work successfully delivered a fully functional hyperspectral microscopy platform, from hardware integration to software development. While the initial results highlighted the inherent physical limitations of using label-free HSI on highly transparent, minimally colored biological tissues, they also establish a strong foundation for future optimization. By expanding the wavelength range into the near-infrared and integrating advanced image processing techniques, this non-invasive technology has high potential for detecting pathological signatures in broader biomedical research.

References:
1. A. Bhargava et al. Hyperspectral imaging and its applications: A review, Heliyon 10, e23999 (2024).
2. N. Bendel et al. Detection of Two Different Grapevine Yellows in Vitis vinifera Using Hyperspectral Imaging, Remote Sensing 12, 4151 (2020).

Contents

Chapter 1

Introduction and Research Background

1.1 Hyperspectral Imaging

Hyperspectral imaging (HSI), also known as spectroscopic imaging [1], is used in several fields. It has become an efficient tool, for example, in archaeology, food quality [2] and safety control, the military, environmental monitoring, and medical applications [3] [4].

This method combines two-dimensional spatial information with spectral information. It generates a three-dimensional, so-called hyperspectral data cube (or hypercube), as shown in Figure 1.1, where we can order for each pixel of the two-dimensional image a spectrum.

In Figure 1.1, you can also see the comparison with a simple RGB camera. With an ordinary camera, you obtain red, green, and blue wavelength components at a given intensity, whereas with a hyperspectral camera, you obtain the continuous wavelength spectra of each pixel (within a certain resolution). In this way, we arrive at a three-dimensional dataset where the measured intensity depends on three components two spatial and one spectral: $I(x, y, \lambda)$ which can be formally described as a function $I : \mathbb{R}^3 \to \mathbb{R}$.

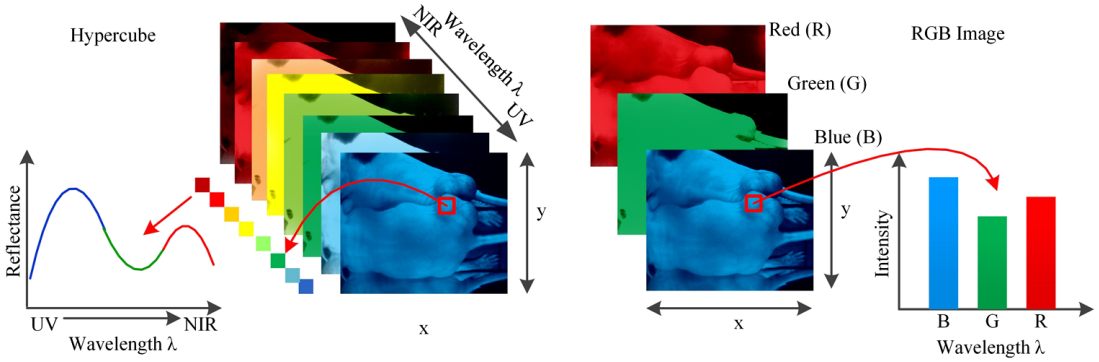

Figure 1.1: Comparison between a hypercube and an RGB image. The hypercube contains a two-dimensional image at each wavelength, and for a single pixel it provides a continuous spectra. In contrast, the RGB image only has three wavelength components: red, green, and blue [5].

As light enters the object, it undergoes absorption, reemission and multiple scattering due to the inhomogeneity of the object. (Scattering occurs where there is a spatial variation in the refractive index [6].) Therefore, the reflected, transmitted, or emitted light provides a fingerprint of the object and carries valuable information.

HSI sensors typically capture near-infrared (NIR), visible, and short-wavelength infrared spectra within the range of $0.4 - 2.5$ μm [1].

Four primary acquisition modalities are employed in hyperspectral imaging: point scanning, line scanning, spectral scanning, and snapshot, as illustrated in Figure 1.2. Point scanning involves sequentially scanning each pixel along the x and y spatial dimensions and acquiring the corresponding spectral data. Line scanning acquires spectral information along a single spatial axis. Spectral scanning captures images at discrete spectral bands sequentially across the wavelength dimension. Snapshot imaging simultaneously captures the complete hyperspectral data cube in a single acquisition.

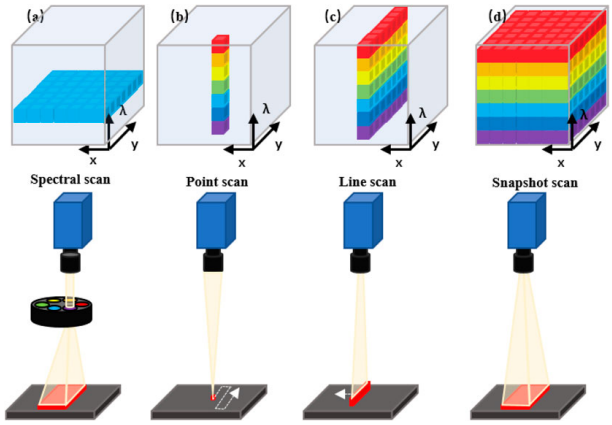

Figure 1.2: Acquisition approach of the hyperspectral data cube. (a) Spectral scanning (b) Point scanning (c) Line scanning (d) Snapshot [7]

An intriguing example of HSI application is found in medicine, because it enables noninvasive diagnosis. Within tissue, light scatters due to the inhomogeneity of biological structures and is absorbed by hemoglobin, melanin, and water as it propagates through the tissue [5].

1.2 Zebrafish Embryos

Zebrafish (Danio rerio) embryos are important model animals in research. They are transparent during the embryonic stage (at the larval stage, pigmentation begins to develop), which enables easy examination of their organs. Their rapid development - one pair can produce 200-300 embryos per week - allows for high reproducibility of measurements. Because of the high reproduction rate and their size (one zebrafish embryo measures about $1 - 2$ mm), it is easy to examine many embryos in a short time, what allows to make conclusions based on statistical analysis. They develop externally, which allows researchers to easily examine embryos without harming the adult specimens.

Furthermore, their genome structure is 70% similar to humans [8], making them useful for studying human genetic diseases [9]. After the 3th day of fertilization the most important organs are developed in the embryos, like eyes, brain, heart, spine, muscles and inner

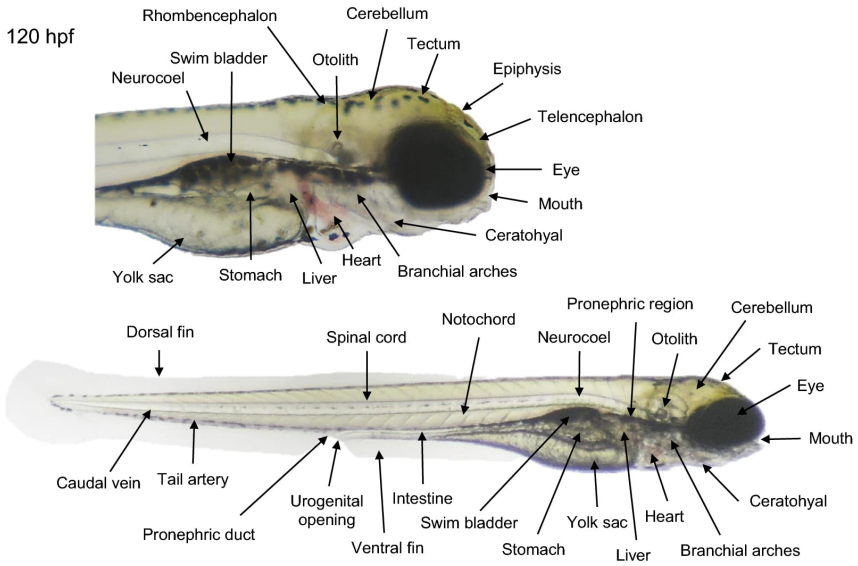

Figure 1.3: Morphology of normal zebrafish embryo at 120 hpf [13]

organs. On Figure 1.3 you can see the morphology of a normal zebrafish embryo after the 5th day of fertilization. This rapid development also helps in efficient examination. According to EU Directive 2010/63/EU, zebrafish early life stages are not protected as laboratory animals, and only become regulated from the point when they are able to swim and feed independently (7 days after fertilization) [10].

Because of these advantages, the field has significantly grown in recent years in radiobiologycal studies too [11] [12]. Zebrafish embryos are used in drug discovery and in comparement of different irradiation methods. Their rapid development also facilitates studying the expression of oncogenes (cancer-causing genes), which can be controlled in specific organs.

In this work, my goal was to examine zebrafish embryos using hyperspectral microscopy. This is a challenging task because the specimens are very small (approximately 3-5 mm in length) and are either highly transparent or strongly pigmented. As a result, accurately measuring light scattering within the tissues is difficult.

1.3 Spectral Angle Mapper

Spectral Angle Mapper (SAM) is a supervised classification algorithm used primarily for analyzing remote sensing and hyperspectral images to extract thematic information [14]. It works by measuring the spectral similarity between two spectra: a pixel's spectrum (test vector: $\mathbf{t}$) and a predefined reference spectrum (reference vector: $\mathbf{r}$). SAM treats each spectrum as a vector in an n-dimensional space, where n represents the number of spectral bands in the image. By calculating the angle between the test vector and the reference vector (see in Equation 1.1), it determines their similarity. Pixels that exhibit a minimum or zero spectral angle compared to the reference spectrum are assigned to that specific class.

$$\alpha = \arccos\left(\frac{\mathbf{t} \cdot \mathbf{r}}{\|\mathbf{t}\|\|\mathbf{r}\|}\right) \tag{1.1}$$

A major advantage of the SAM algorithm is that it relies solely on the shape of the spectra rather than their length or magnitude. This makes the method insensitive to unknown gain factors, meaning it can handle variations in illumination equally and effectively. However, the algorithm does have some limitations. Because it is a linear model, SAM does not perform well when different classes overlap with one another. Additionally, if the threshold used for classification is modified, it can increase the probability of incorrect object detection.

Chapter 2

Optical Design of the Hyperspectral Setup

The design of a hyperspectral camera begins with defining the required system specifications. One of the most crucial parameters is the spectral range. Different materials exhibit distinct spectral signatures across various wavelength bands, so the spectral range covered by a hyperspectral camera defines which substances it can identify and analyze effectively. In biological samples many substances have distinct spectral characteristics in the VIS and NIR region. Therefore, the goal is to build a camera sensible around the $450-800$ nm spectral range. Another reason is that CMOS and CCD cameras have a big quantum efficiency in this part of the spectrum, which makes it easier to make examinations here.

I have designed the camera with regard to two main factors: spectral and spatial resolutions. Spectral resolution represents the capability of a hyperspectral camera to differentiate between two different wavelengths. A higher spectral resolution allows the camera to detect subtle differences in the spectral properties of a material, which is essential for spectral marker determination. $1-3$ nm allows enough spectral information in the ~ 300 nm wide range. Also oversampling can cause problems like taking too much time scanning the pictures. Spatial resolution is defined as the minimum distance between two points that can be distinguished as separate, or more formally, the full width at half maximum (FWHM) of the point spread function (PSF). As an initial step, I constructed a hyperspectral camera with a spatial resolution of 150 µm. For microscopic examination of embryos sized $3-5$ mm, I redesigned the camera to provide resolution down to 10 µm.

2.1 Hyperspectral Camera

The optical design of the hyperspectral camera is shown in Fig. 2.1. I diffusely illuminated the object with a white ring LED source and collected the scattered light using a lens. (Later, I used transmissive illumination as well). This objective lens is followed by a folded 4f imaging system, with a reflective grating placed in its Fourier plane. A slit is used to select a vertical strip, and scanning is performed by moving the objective lens. In this configuration, the image forms on the slit, and the magnification between this intermediate image and the image at the camera can be adjusted by changing the focal lengths of the collimating and focusing lenses.

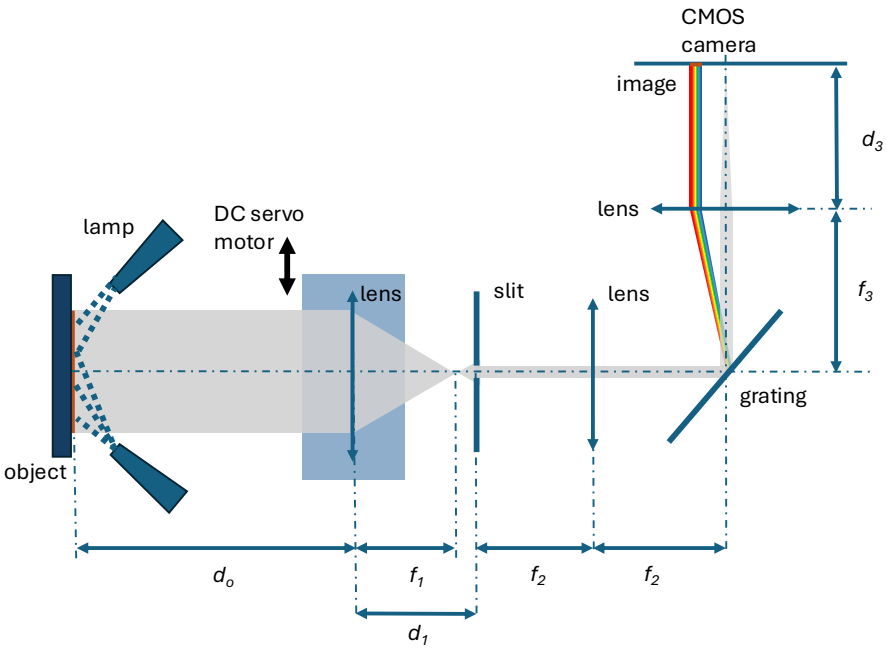

Figure 2.1: Schematic diagaram of the hyperspectral camera.

The image, with wavelength and spatial position along the horizontal and vertical axes respectively, is recorded by a camera. The system parameters were optimized to meet the required specifications, primarily in terms of wavelength range and object size. The design calculations were carried out using the paraxial approximation. The selected parameters of the optical elements are listed in Table 2.1, and the chosen components are summarized in Table 2.2. All lenses used in the system are achromatic, and the objective lens has a larger diameter to increase the numerical aperture. The grating line density, focal lengths, and object distance were chosen to achieve a spectral range of approximately 260 nm and sufficient spatial resolution (around 150 µm).

Description		Symbol	Value [mm]
Focal legth of the	objective lens	f_1	50
	collimating lens	f_2	100
	focusing lens	f_3	50
Diameter of	objective lens	D_1	30
	collimating lens	D_2	25
	focusing lens	D_3	25
Object distance		d_0	500
Image distance from	objective lens	d_1	55.6
	focusing lens	d_3	55.6

Table 2.1: Parameters of the hyperspectral camera.

I used a HeNe laser beam to precisely align the optical components along a common optical axis. Proper collimation of the beam onto the grating is crucial - if the beam is not well collimated, the full width at half maximum (FWHM) of the modulation transfer function (MTF) in the design becomes significantly larger.

Component	Part used
Objective Lens	Edmund Optics 49-371
Slit	Thorlabs S50HK (50 µm width)
Collimating Lens	Edmund Optics 49-360
Reflective Diffraction Grating	Edmund Optics 64-402 (150 gv/mm)
Focusing Lens	Edmund Optics 49-356
Camera Sensor	DMK 33UX273
Motor	KDC101 DC Servo Motor Controller

Table 2.2: Components of the hyperspectral camera.

For calibration, I used two different interference band-pass filters (630 nm and 720 nm), and later, for more precise calibration, I used a neon gas discharge lamp source. The capture settings are listed in Table 2.2a. Figure 2.2b shows the setup in the laboratory environment.

	Setting
Image size	(1280, 960) pix
Scanning velocity	0.2 m/s
Scanning range	3 mm
Scanning time	15 sec
Wavelength range	430-690 nm
Spatial resolution	150 µm
Wavelength resolution	1.2 nm

(a) Capture settings of the hyperspectral camera.

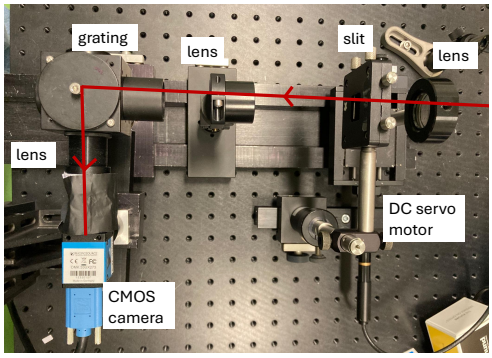

(b) Optical setup of the hyperspectral camera in laboratory environment.

Figure 2.2

After data acquisition, I reconstructed the RGB image captured of an object, as shown in Figure 2.3a. The intensity was corrected using the camera's sensitivity curve.

Figure 2.3: a) Reconstructed RGB image from object (colorful parrot) with a hyperspectral camera, b) A photo made with a phone.

2.2 Hyperspectral Microscope

For a microscopic setup the object distance reduces a lot, and I wanted to change the parameters to have a magnification around two. For imaging zebrafish embryos, they often use 2X, 5X and 10X magnification (in Szeged). Therefore I tried to achieve 2-3X magnification with a resonable $< 10\mu m$ spatial resolution.

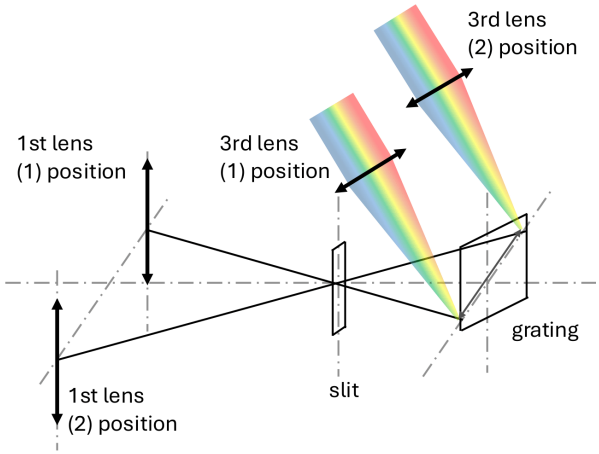

Figure 2.4: Spectral overlap on the camera caused by changing the objective lens positions.

I noticed during building the new microscopic configuration, that when the first lens is in different positions (Figure 2.4), the wavelength spectras would slide into each other on the camera sensor. I made a measurement concerning this phenomena, where I used a 630 nm and a 720 nm filters, and I saved the pictures taken by the camera in different objective lens positions. The summed profiles of the measured intensity can be seen in Figure 2.5. To address this issue, I moved the sample rather than the first lens and used a transmittission grating. Because sample motion is required anyway, moving the first lens is not necessary. The picture with the new optical setup in the laboratory is in Figure 2.6.

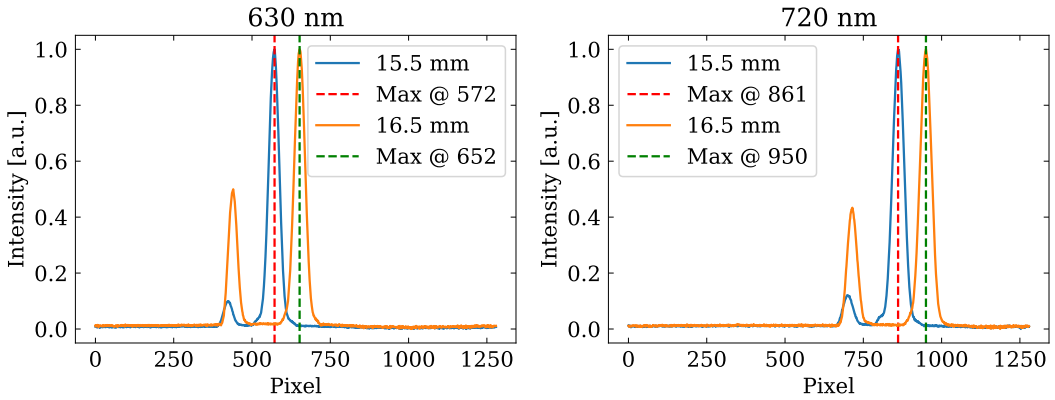

Figure 2.5: Summed camera spectra of 630 nm and 720 nm filters at different objective lens positions (15.5 and 16.5 mm).

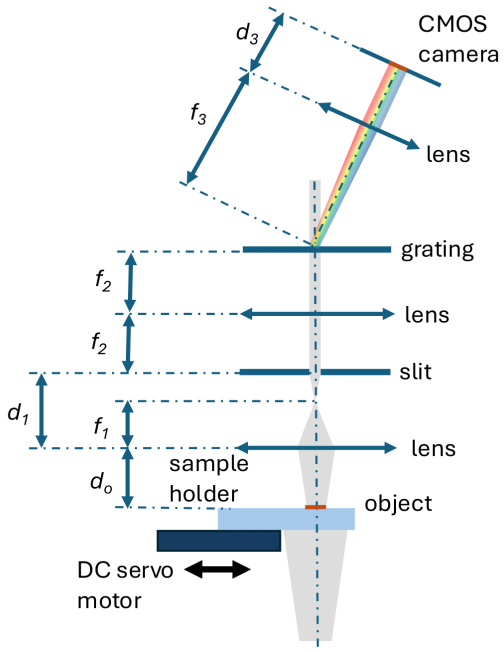

(a) Schematic diagram of the hyperspectral microscope (with trasmitted illumination).

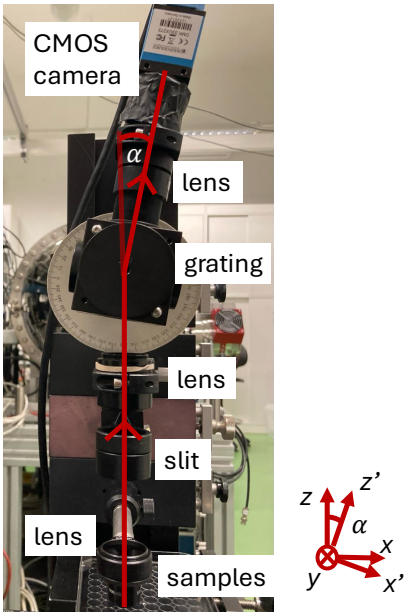

(b) Hyperspectral microscope setup in laboratory environment.

Figure 2.6: Hyperspectral microscope schematic and experimental setup.

Besides that, I made the whole system vertical using rail structured elements, for easy alignment. Vertical setup is needed, because the specimens will have to lie horizontally. The schematic diagram of the optical system can be seen in Figure 2.6a and the parameters in Table 2.3.

Description		Symbol	Value [mm]
Focal legth of the	objective lens	f_1	20
	collimating lens	f_2	50
	focusing lens	f_3	50
Diameter of	objective lens	D_1	12.7
	collimating lens	D_2	25.4
	focusing lens	D_3	25.4
Object distance		d_0	30
Image distance from	objective lens	d_1	60
	focusing lens	d_3	60

Table 2.3: Parameters of the hyperspectral microscope.

For the specific components I chose the ones listed in table 2.4. For the objective lens I chose an achromatic triplet, to reduce the chromatic aberrations. For the collimating and focusing lens I have chosen acromatic doublets. A 20 µm wide slit was used, to increase the spatial resolution.

Component	Part used
Objective Lens	Thorlabs TRS127-020-A-ML (triplet)
Slit	Thorlabs S20LK (20 µm width)
Collimating Lens	Thorlabs AC254-050-AB
Reflective Diffraction Grating	Thorlabs GT25-03 (300 gv/mm)
Focusing Lens	Edmund Optics 49-356
Camera Sensor	DMK 33UX273
Motor	KDC101 DC Servo Motor Controller

Table 2.4: Components of the hyperspectral microscope.

The capture settings related to the acquisitions and the system properties will be discussed later (in Chapter 5), and are listed in Table 5.1. The camera's sensor size is 5 mm, and I aimed to capture a 300 nm wide spectrum on it. By choosing $a = 3333.3$ nm with $f_{3,2} = 50$ mm, the theoretical separation at the camera between λ_1 and λ_2 will be 4.6 mm.

From measurements, on the camera (5 mm sensor size) I obtained a 300 nm wide spectrum on the sensor: from $\lambda_1 = 495$ nm to $\lambda_2 = 795$ nm. A transmission grating is preferable because an inline optical configuration can reduce aberrations such as astigmatism. With this setup, I could achieve a 300 nm wide range on the camera.

Using 2.1. grating equation α - the diffraction angle for $\lambda_0 = 550$ nm can be calculated.

$$a \cdot (sin\theta_m + sin\theta_i) = m \cdot \lambda \tag{2.1}$$

This equation states, that a grating with spacing a will deflect the light at θ_m, where $m = 1$ is the diffraction order, and θ_i is the incident beam's angle. For this setup $\theta_i = 0°$, and knowing the grating period $\theta_1 = \alpha = 9.5°$.

To assess the imaging properties of the current setup, I performed a Zemax OpticStudio simulation. I investigated the spot diagrams for different field points (2.8), and measured other characteristic properties of the device, which are summarized in Table 2.5. I imported the Zemax lens files from the corresponded website. Three wavelengths were used (400, 550, 700 nm), and the object-space numerical aperture was NA = 0.2. The system layout is shown in Figure 2.7. Before and after the grating I used coordinate break, for accounting the diffraction angle. I tilted the coordinate system using the Chief Ray, and after that, all subsequent coordinates followed the primary wavelength.

I optimized the inter-element spacings using a merit function with bounded variables, targeting the minimum RMS spot radius. Field points were defined to match the plate size (5 mm diameter).

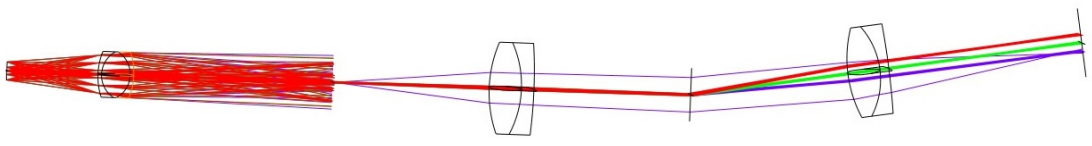

Figure 2.7: Zemax sequential 3D layout of the hyperspectral microscope system.

Parameter	Symbol	Value
Effective focal length	EFL	−19.20 mm
Magnification	M	2.47
Object space numerical aperture	NA_{obj}	0.20
Image space numerical aperture	NA_{img}	0.082
Working F-number	F/#	7.32

Table 2.5: Hyperspectral microscope characteristics.

Figure 2.8 shows polychromatic spot diagrams for several object points. When scanning perpendicular to the slit, the blue component appears and can degrade image quality, however, I made the calibration that starts from 495 nm, so this effect did not contribute to the recorded data. The system is not diffraction limited.

On the image plane, a 1 nm wavelength change corresponds to 0.0644 µm, and from later the measurement I got 0.0681 µm separation on the camera sensor. The paraxial magnification reported in the system data is 2.47, and I will show in Section 5 that the system's magnification in practice is 2.42.

F/# controls overall light throughput, depth of field, and the ability to produce contrast at a given resolution (F/# = 1/2NA). A value of working F/# = 7.32 is relatively high, meaning lower light throughput but a larger depth of field, which is important because precise focusing is challenging in this setup.

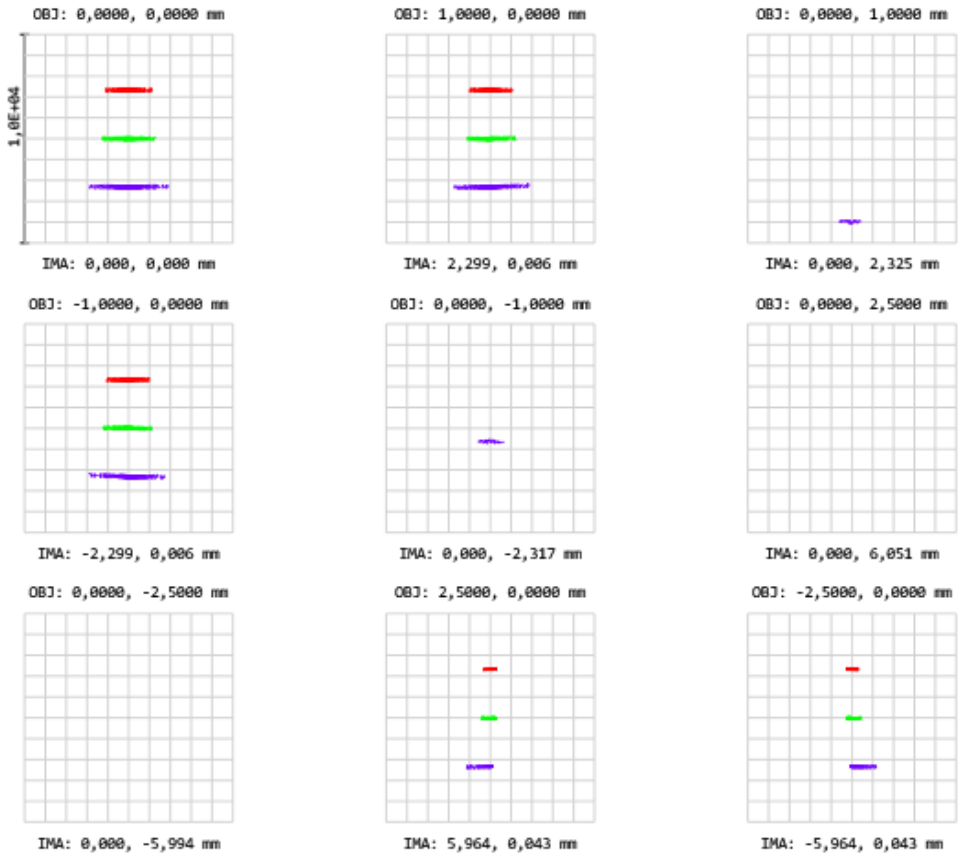

Figure 2.8: Polychromatic spot diagrams at multiple field points across a 5 mm field. Wavelengths: 400, 550, 700 nm.

2.3 Illumination

Illumination is a critical component of hyperspectral imaging systems. After illuminating the object or tissue, the reflected, scattered, or transmitted light enters the optical system. The goal is to measure the difference between the illumination spectrum and the measured spectrum, which changes slightly due to interaction with the sample.

The illumination spectrum should be broad, and the more homogeneous it is, the easier it becomes to normalize the measurements. It is also crucial that the illumination remains stable, any change in wavelength during measurement can lead to systematic errors.

Transmissive and refractive illumination gives us different properties of the sample under investigation. To understand better the consequences of these and see which will give a more useful result, I tried both and compared them. With transmittive illumination, we measure the transmitted light, in different wavelengths. Absorption happens what can be described with the Lambert Beer's law. Here the fundamental beam is also strongly present in the measured data. The thicker and darker parts of the fish don't carry data, since the light will not pass through them. In microscopic setups, they use transmissive illumination to have a larger contrast.

Using refractive illumination, the eye of the embryo could be also studied, what is a high preference in biological studies. Altought we can assume that the contrast will be lower.

2.3.1 Transmissive Illumination

I tested several illumination setups. Initially, I used a white ring-shaped LED light. Its advantages include low cost, minimal heat production, and long lifetime. However, it also has drawbacks, such as uneven signal intensity what caused saturation issues due to its strong blue peak around 450 nm.

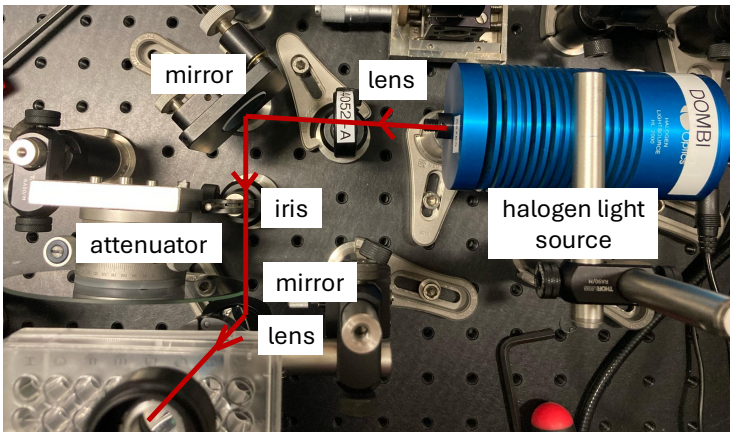

Figure 2.9: Laboratory setup of the halogen-based illumination system.

Next, I used the Samba 450 Leukos laser. This provides continuous spectra between 450 and 2400 nm and delivers high power. The drawback of using this laser as an illumination source is its high spatial coherence, which produces interference patterns in the image. Because a fish is an amplitude object rather than a phase object, using an incoherent light source is a better choice. Another disadvantage of this laser is its high cost.

Several studies have discussed optimal illumination sources for hyperspectral imaging [15]. According to these studies, incandescent lamps are among the best options. I used a halogen lamp, which is an improved form of an incandescent lamp.

This light source shows no significant spectral peaks across its operating range, making it easier to neutralize its influence during data analysis and hyperspectral calculations. It is inexpensive, emits a continuous spectrum between 400 and 2500 nm, and is non-coherent. Halogen lamps are often compared to blackbody emitters.

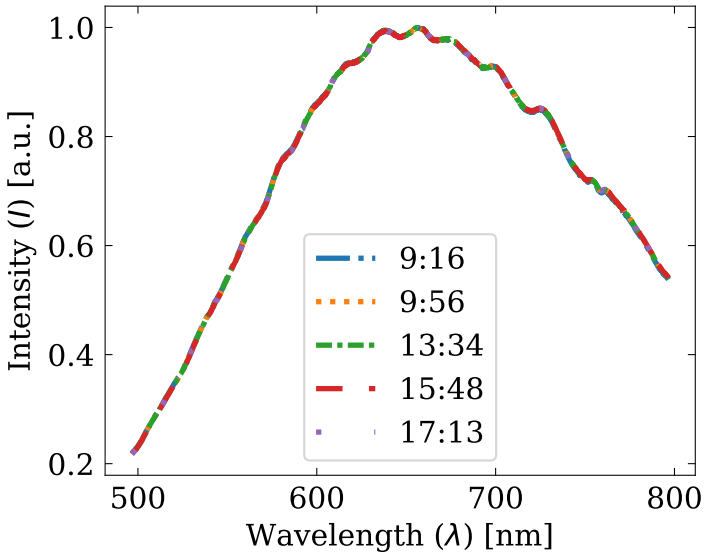

Figure 2.10: Halogen lamp stability measurement: normalized illumination spectra over time.

A halogen lamp contains a tungsten filament through which an electric current passes. The filament heats up and emits light. Unlike traditional incandescent lamps, halogen lamps operate at higher temperatures, increasing their efficiency.

Zebrafish embryos are transparent, allowing an exceptional level of direct observation during embryonic stage. The zebrafish body thickness in the trunk region is approximately 0.4-0.6 mm. The eye, swim bladder, and stomach strongly attenuate the light, resulting in low measured signal and low SNR. Other parts of the fish were relatively transparent.

I used a Halogen Light Source HL-2000 from Ocean Optics. It produces light in the range of 360 nm-2400 nm with an output power of 7 W. An attenuator was used before the source to control the illumination intensity and achieve optimal image contrast.

Before measurements, I allowed the light source to stabilize for approximately five minutes after switching it on. In the laboratory, I designed a setup to obtain reproducible measurements, shown in Figure 2.9.

After the halogen light source, I placed a Thorlabs LA4052-A lens with a 35 mm focal length to collimate the beam toward a mirror. Then, an adjustable iris was used to control the illumination aperture. Subsequently, a mirror directed the beam vertically to a focusing lens (focal length 15.1 mm, asphere).

The sample holder contained 5 mm diameter circular wells. I adjusted the illumination distance and numerical aperture to illuminate an entire well uniformly.

Based on the focusing lens properties, the illumination systems numerical aperture (NA) was 0.4, while the optical systems NA was 0.2. A larger illumination NA is beneficial because it allows image acquisition even if the samples are not perfectly centered within the circular wells.

Since the goal was to measure the spectrum for each pixel, maintaining consistent illumination over time was essential. To ensure this, I performed stability measurements. On the days when sample acquisitions were conducted, I regularly measured the illumination spectrum to determine whether calibration corrections were necessary.

The normalized illumination spectra over time are shown in Figure 2.10. This intensity is the product of the illumination light source spectrum, trasmittances of the optical components and the sensitivity of the detector. The intensity was normalized to the maximum. As the Figure also shows, there is no need for corrections, because the spectrum of the halogen illumination is stable.

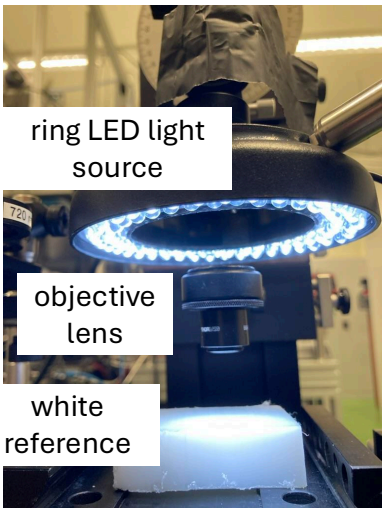

(a) Laboratory setup of the refractive illumination system using ring LED light source.

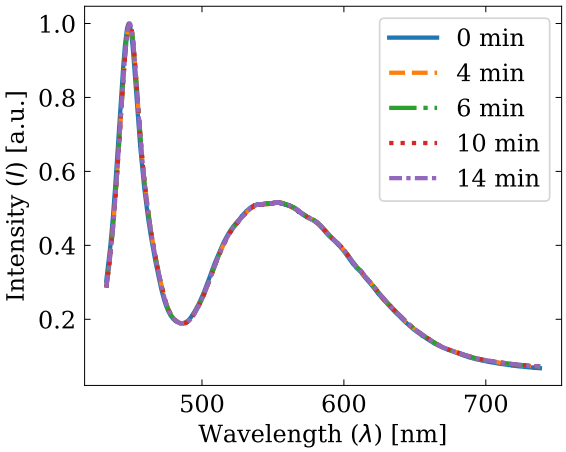

(b) Ring white LED lamp stability measurement: normalized illumination spectra over time.

Figure 2.11

2.3.2 Refractive Illumination

For refractive illumination (Figure 2.12), a ring light (Aven 26200B-214 LED Ring Light) was used as Figure 2.11 also shows. The circular geometry enables illumination from multiple angles, thereby reducing shadowing effects. The height of the ring was adjusted to achieve the most homogeneous illumination. This configuration, together with the tilted orientation of the LEDs, helps to minimize total reflection (which would occur under incidence from above) as well as shadowing (as would be the case with bottom illumination). Although the spectral output of an LED source is less uniformly distributed across wavelengths compared to that of a halogen lamp, this geometry was more easily implemented. The ring light provides an intensity of 300 lumens and has a color temperature of 8000 K.

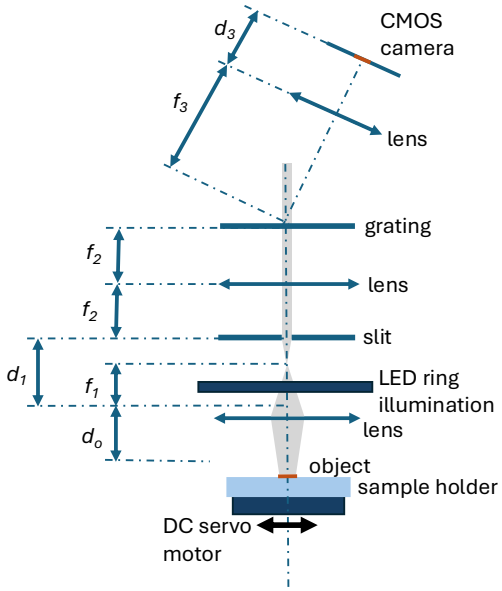

(a) Schematic diagram of the hyperspectral microscope (with reflactive illumination).

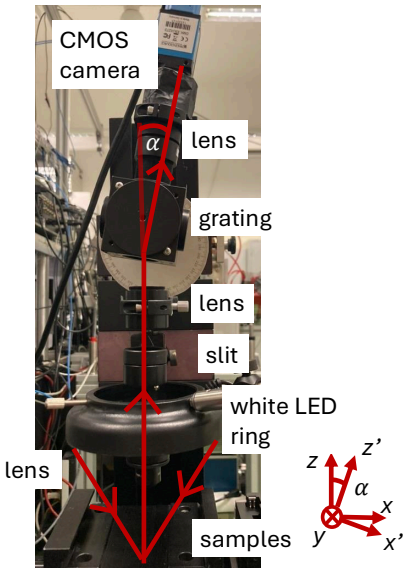

(b) Hyperspectral microscope setup in laboratory environment (with reflactive illumination).

Figure 2.12

Chapter 3

Software Development

This chapter explains the software I developed to control the hardware of the system and interact with users. The main hardware parts are a piezo stage controlled by a servo motor (KDC101 DC Servo Motor), and a camera (DMK 33UX273). The software manages these devices using separate classes and offers a user-friendly interface to operate everything easily during measurements.

3.1 Communication with the Servo Motor and Camera

The software works by controlling two main devices: the servo motor and the camera. The `PiezoStage` class controls the motor. It can move the motor to exact positions, move it relative to its current place, and perform a homing sequence to reset position. It also controls how fast the motor moves.

The `Camera` class manages the camera. It can start the camera, set parameters like exposure, gain, image size, and take images.

These two are combined in the `ExperimentSystem` class, which can move the motor while taking pictures simultaneously. Using this scanning method, the slit selects different parts of the image, and by saving the wavelength - vertical position images at each lateral position, a hyperspectral data cube is formed. The program can save the images, motor positions and metadata in structured files (HDF5 files) for later use.

Component	**Main Features**
PiezoStage Class	Find and connect to motor devices. Move motor to specific or relative positions. Perform homing to reset position. Set movement speed.
Camera Class	Initialize and open camera stream. Set exposure, gain, and image size. Capture single images.
ExperimentSystem Class	Control both motor and camera together. Scanning: move motor and capture images simultaneously. Save data including images, metadata and motor positions in files.

Table 3.1: Main software components for communication with the devices

3.2 Graphical User Interface

The graphical user interface (GUI) is made with PyQt5. It allows users to control the camera and the motor easily, and to see the live camera view. The GUI is organized across three screens, from which the user can choose: the Home page, Photo page and Piezo page.

In the Home page (see in Figure 3.1) one can initialize the camera and motor, make a scanning method, set the parameters of the scanning, save and visualize the data. During the scanning process, with the help of the DC servo motor, the sample moves from position x_1 to x_2 while the camera continuously captures images, rather than using a step-and-shoot method, enabling faster measurements.

Because with different speeds a distortion can occure in the image, I also made an aspect ratio checkbox, to easily visualize the distorted data too. After saving the scanned data, to a folder, you can easily choose from that folder what hyperspectral cube do you want to visualize. An interactive matplotlib plot will show the captured images in different wavelengths, and the user can change betwen the wavelengths using a slidebar. This quick feedbacked helped wether to make the measurements again, or not. The easy plot button visualized the picture in six different wavelengths at the same time, for quick comparism.

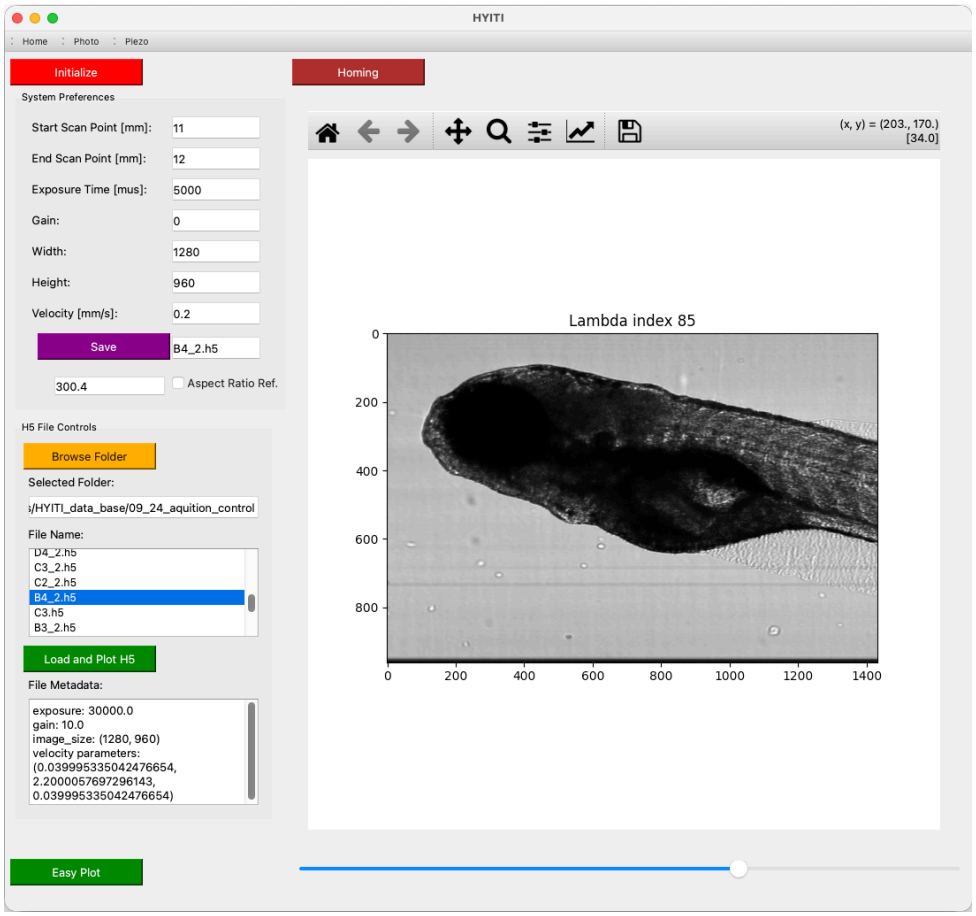

Figure 3.1: Homapage of the program.

The second toolbar is the Photo toolbar. Here, users can set camera parameters and adjust settings such as exposure time, gain, and image size using text boxes (as shown in Figure 3.2a). They also have the option to start or stop the live view, as shown in Figure 3.3. This feature was important for aligning the setup, which I will discuss in more detail in Chapter 4.

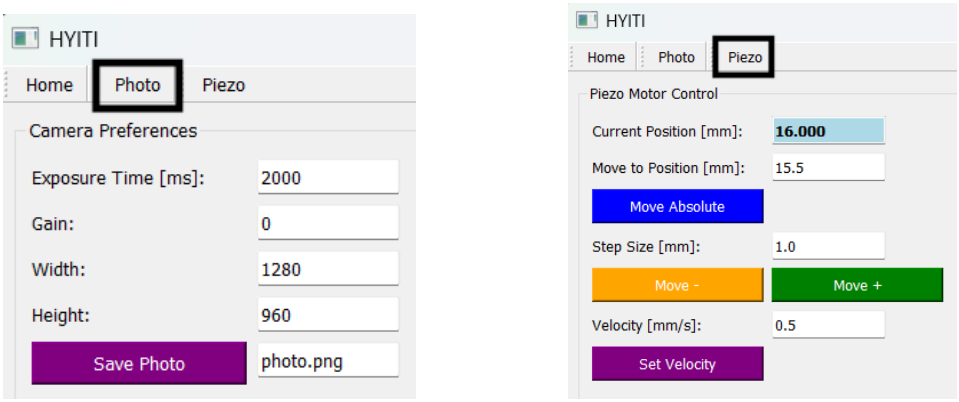

(a) Photo page, camera settings.

(b) Piezo page, motor settings.

Figure 3.2

The livestream operates using threads, and the mechanism is illustrated in Figure 3.4. The key point is that image storage and plotting occur in parallel, meaning the images are not necessarily previewed immediately after being captured. Although this feature is not essential for my current application, it could be useful in the future when handling large scanning datasets, as it allows images to be stored and previewed later. I aimed to make the system as modular as possible.

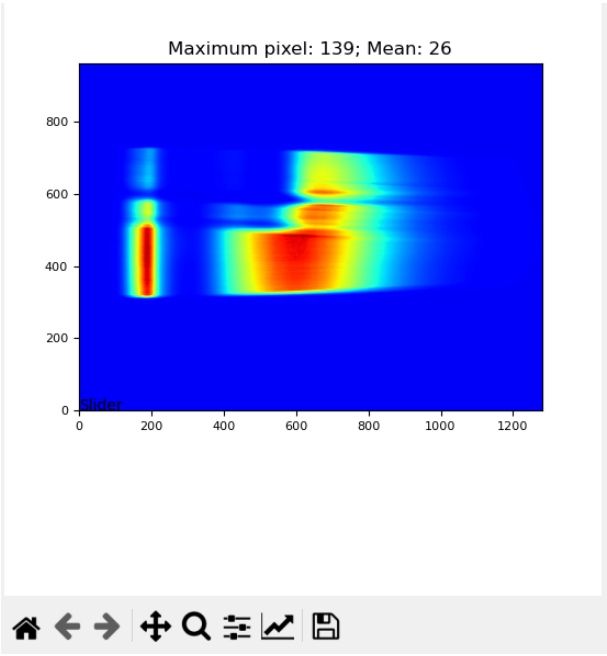

Figure 3.3: Camera live view.

On Figure 3.4 I illustrated with a flowchart the process of live camera image acquisition and display. The system starts from the MAIN control, where the preview thread is launched. Inside the preview thread, the camera stream is set up, and a loop (grabFromCamLoop) continuously captures photos from the camera, signaling when a new image is ready ("new Pic"). Simultaneously, the previewShowloop thread waits for this new image event to update the display by setting the image data on a visualization canvas ("imshow canvas"). The loops continue running until the streaming is stopped or an exit signal is received, at which point the stream ends, and the threads break. This threaded design ensures smooth, real-time camera preview and responsive GUI operation without blocking.

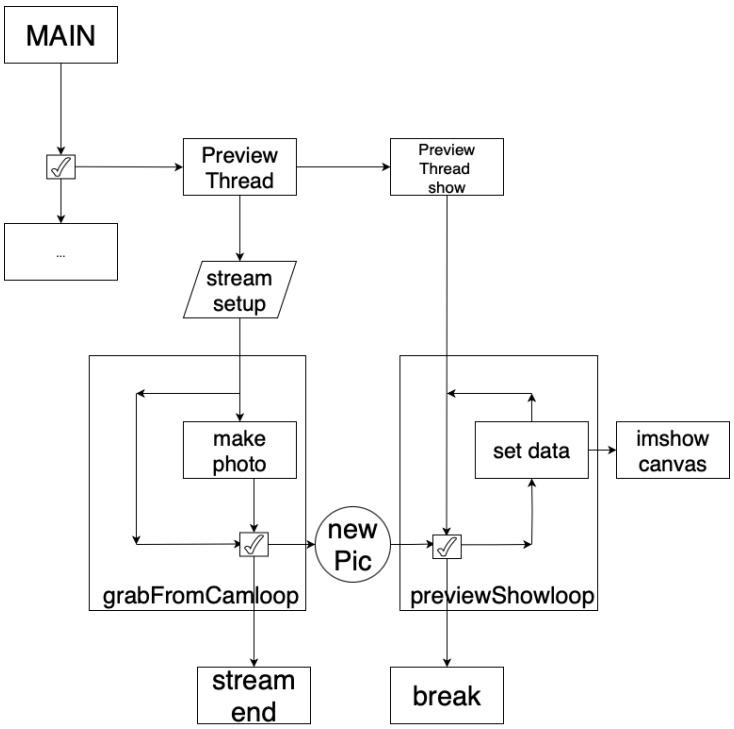

Figure 3.4: Flowchart for real-time camera preview and display using threads.

The last toolbar, called the Piezo Page, provides dedicated control over the piezo motor. Even though motor settings can also be adjusted through the scanning method, it proved useful to have direct, independent control. During the measurements, it was often necessary to reposition the motor manually to locate the next specimen efficiently. This functionality greatly facilitated the measurement process and improved the alignment procedure. This is the reason why I implemented Piezo Toolbar, illustrated in Figure 3.2b.

In Table 3.2, the main features and components of the GUI are summarized. The software was developed to function on both macOS and Windows within a laboratory setting.

GUI Feature	**Description**
Home Page	Central control page for system initialization, scanning, and data visualization.
Scanning Interface	Allows configuration of scan parameters (start/end position, velocity) and executes synchronized image capture. Real-time position tracking. Spectral binning for data compression.
Image Saving Functionality	Saves current scan data to HDF5 format, including all metadata (exposure, gain, position, etc.), with file path selection and confirmation.
Easy Plot Dialog and Slider	Slider: interactive visualization tool for hyperspectral data, Easy Plot: plotting pictures in 6 different wavelengths next to each other.
Photo Page (Camera Preview)	Provides real-time camera live view, supports exposure/gain adjustment and single photo capture.
CamViewer Class	Displays live camera feed with thread-based smooth updates.
Camera Parameter Controls	Editable fields for exposure, gain, and resolution settings, updates camera parameters directly.
Piezo Page (Motor Control)	Manual control of Thorlabs piezo stage, includes absolute and relative motion, homing, and velocity configuration. Real-time position monitoring.
Toolbar Navigation	Multi-page navigation between modules (Home, Photo, Piezo), includes status indicators.
Helper GUI Classes	Standard buttons, text fields, and labels for consistent look.

Table 3.2: Key user interface components of hyperspectral camera and microscope.

Chapter 4

Alignment of the Measurement System

The last prototype of the hyperspectral microscope that I built in the lab was vertically oriented. On a rail-based structure, I was able to set easily the proper distances between the optical elements.

First, I placed every component at the specified distances to check whether everything could be positioned next to each other mechanically. For more precise alignments, I did not need to remove all the components, because, for example, I could easily take the grating out of its case or tilt the second lens down.

I summarized every component's alignment possibilities (or degrees of freedom) in Table 4.1 based on the picture and coordinate systems you can see in Figure 2.12b. After the grating I used the sign ' for the coordinate system transformation, because I chose the new optical axis along the diffraction orders.

Component	Directions
Objective (1st) Lens	-
Collimating (2nd) Lens	x
Focusing (3rd) Lens	-
Slit	z
Camera	z'
Sample holder	z, x

Table 4.1: Small alignment possibilities of the components or degrees of freedom along the (x, y, z) or after the grating (x', y', z') directions.

Using a HeNe laser, I ensured that every optical component was aligned at the center of the optical axis. This way, all components were positioned at the same height. The next step was to establish the illumination and imaging path for the hyperspectral microscope. I used the halogen lamp as the illumination source (later I also made measurements with LED sources). I positioned the first lens at the correct distance from the object plane to form a focused image of the sample on the slit, what could be visually observed, and I placed the slit in this position.

Next, I mounted the second lens in the system to collimate the light before it reached the diffraction grating's position (here I didn't use the grating). The collimation was verified by observing the beam at a larger distance and I ensured that no vignetting occurred,

and that the beam fully filled the aperture of the optical elements. When properly aligned, the Fourier transform of the image became visible on the grating plane, confirming the correct optical configuration.

Once the collimated beam reached the grating position, I positioned the third lens at the defined distance behind it. Then, to achieve a sharp image, I adjusted the position of the camera along the optical axis until the sample placed at the object plane appeared focused on the detector. These focusing adjustments were initially performed without the grating and without the slit in position.

After completing this prealignment, I reinserted the slit and ensured it was perpendicular to the light propagation direction. The diffraction grating was then mounted into its cage. Because the optical cage system beyond the grating was monolithic, rotating the grating cage around its axis also rotated the attached lens and camera, maintaining their relative geometry.

Finally, I fine-tuned the grating (and the things after that) orientation by observing the first-order diffraction on the camera. I checked with filters (630 and 720 nm central wavelength) or occasionally with an LED that had a known spectrum, which part of the spectrum is on the camera. By adjusting the gratings rotation angle, I could select the desired spectral region to observe. After completing this alignment, I rotated just the grating until its normal vector became perpendicular to the optical axis.

Chapter 5

System Properties

5.1 Resolution

We can distinguish between two types of resolution when talking about hyperspectral camera or microscope: spatial and spectral. First, I will define the device's spectral resolution.

The factors that can limit spectral resolution include the grating, pixel size, and signal-to-noise ratio (SNR). The illumination source is continuous, so it does not impose any limitation.

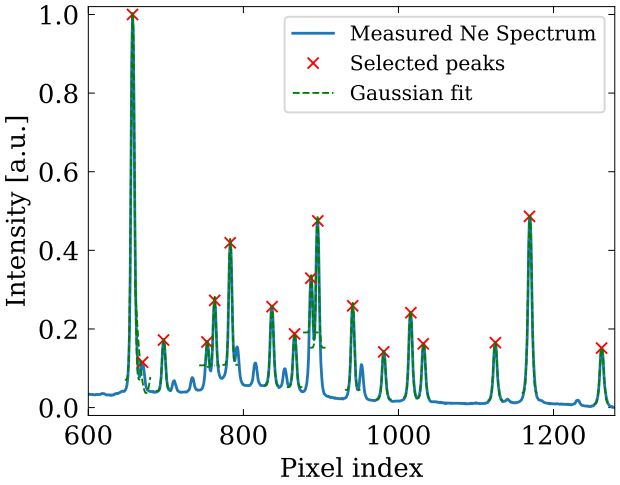

Figure 5.1: Gaussian fitting of selected peaks from the Ne spectrum.

The minimum resolvable wavelength for a diffraction grating is shown in Equation 5.1, where $\lambda = 550$ nm represents the green wavelength, $m = 1$ is the diffraction order, $N = 300$ gv/mm, and $d = 20$ mm is the size of the illuminated region on the grating. From this, we obtain $\Delta\lambda = 0.09$ nm.

$$\Delta\lambda = \frac{\lambda}{mNd} \tag{5.1}$$

After performing the calibration with the Ne source, I fitted Gaussian functions to the selected peaks shown in Figure 5.1. I removed poor fits (when a peak overlapped with

another) and chose the median of the FWHMs of the fitted curves rather than the mean, as the median value was higher. The median FWHM was 5.0 pixels. From the calibration line (Figure 6.1b), the slope was $a = 0.23$ nm/pixel, indicating that the resolution achievable with the Ne source spectrum, based on the optical properties, is 1.16 nm.

For this measurement with the Ne spectrum, I used an image size of 1280x960 pixels. However, during data acquisition, it became evident that each data cube would occupy 600-800 MB for a 1.9 mm scan, which is quite large and unnecessary for such high spectral sampling (1280 values). Therefore, after acquiring one dataset, I averaged every 10 consecutive pixels. As a result, the data size was reduced to 128 pixels in the spectral domain, and the file sizes decreased to 175 MB. Consequently, the limiting factor for the spectral resolution became the data size, where one pixel now corresponds to 2.4 nm, defining the spectral resolution of the system.

I determined the spatial resolution of the system without placing the grating in the optical path. For this measurement, I used a sample with a cross pattern. The smallest division was 10 μm, as shown in Figure 5.2.

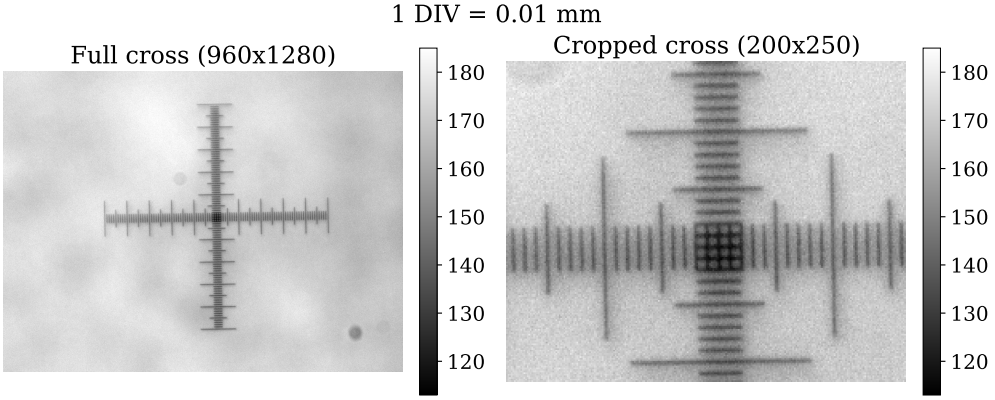

Figure 5.2: Cross-pattern sample used for determining spatial resolution.

I used Fiji software to plot both horizontal and vertical line profiles (Figure 5.3). According to the Nyquist-Shannon sampling theorem, to correctly sample a signal, the sampling frequency must be at least twice the highest frequency present in the signal. In practice, it is advisable to oversample slightly in digital imaging because the optical design is influenced by the modulation transfer function (MTF). As shown in Figure 5.3, the data were oversampled, meaning the sampling interval could be smaller, therefore, the spatial resolution is likely better than what is indicated by this measurement.

In our case, the distance between two dark lines is $d_{min} = 7$ pixels, which corresponds to $x_{div} = 10$ μm in reality. This indicates that the spatial resolution is lower than 10 μm.

I could see that the vertical and horizontal profiles look similar. Altough the vertical resolution is limited with the pixel size, and the horizontal resolution is limited with the slit size. If the slit width is 20 μm and the magnification (see below) is 2.42, that means that $20/2.42 = 8.3$ μm details can be resolved in the fish.

From these data, the magnification of the system can also be calculated. One pixel on the camera corresponds to $p = 3.45$ µm. Therefore, the magnification is:

$$M = \frac{d_{min}\, p}{x_{div}} = 2.42.$$

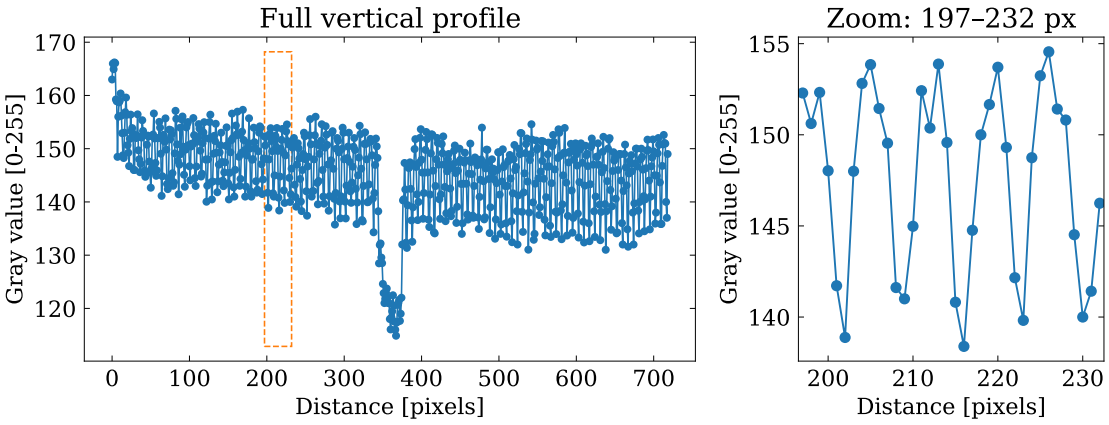

Figure 5.3: Vertical line profiles of the cross-pattern sample.

The capture settings related to the acquisitions and the system properties are listed in Table 5.1. From T_{exp} and v, we can calculate that during exposure, we scan $T_{\text{exp}}v = 6.3$ µm. This means that on the slit because of the magnification, we scan during this exposure time 6.3 µm · M = 15.2 µm. This number should be smaller (or equal) to the slit width (20 µm), to ensure that motion blur does not degrade the spatial resolution.

The camera is 8-Bit monochrome, so we can distinguish 256 different intensity levels in one pixel. This range is sufficient to record subtle intensity differences without producing unnecessarily large data files.

	Setting / Property
Image size	(1280, 960) pix
Scanning velocity (v)	0.09 mm/s
Scanning range (s)	3.0 mm
Exposure	70 ms
Gain	5.0 dB
Spatial resolution	8.3 µm
Wavelength resolution	2.4 nm

Table 5.1: Capture settings and properties of the hyperspectral microscope.

5.2 Spectral Characteristics of Colored Paper

To demonstrate the operation of the microscope, a sheet of paper was colored with red, blue, and green markers. Reflective illumination was used, and the measurements were normalized using the spatially averaged white reference spectrum.

A synthetic RGB composite images were generated by mapping the spectral bands to discrete red, green, and blue display channels, as shown on the left side of Figure 5.4.

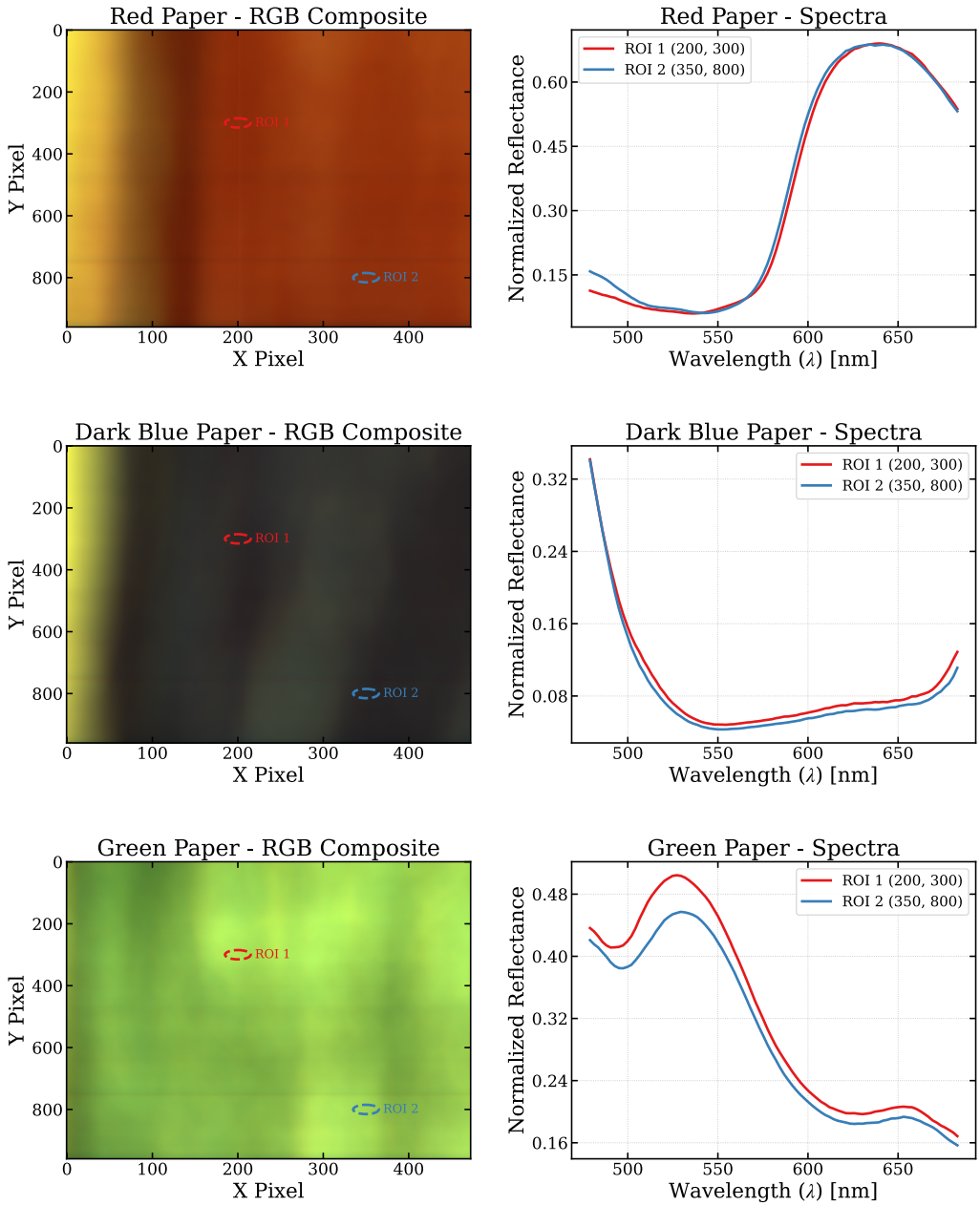

Figure 5.4: Synthetic RGB composites and averaged spectral responses of colored paper samples. The left column shows RGB images reconstructed from hyperspectral measurements of red, green, and blue colored regions. The right column presents the averaged spectra extracted from two selected ROIs for each color sample, demonstrating distinct spectral responses.

The blue colors appear inaccurate mainly because the blue part of the LED illumination was slightly out of the captured spectral range.

Two different ROIs were selected for each sample, and their averaged spectra were plotted, as shown on the right side of Figure 5.4. The distinct spectral curve shapes validate the operation of the hyperspectral microscope and demonstrate its capability for spectral difference detection.

More precise color characterization measurements could be achieved using calibrated color reference samples.

Chapter 6

Measurement Protocol

Calibration is required for any type of spectrometer. I performed two types of calibration: one simple and rapid, and another more precise. For the first method, I used two wavelength filters: one at 630 nm and another at 720 nm. I captured images with the camera, summed each image along the vertical axis, and interpolated the peaks. This yielded a calibration equation, allowing me to convert one axis of the hyperspectral data cube to wavelength.

I also used a more precise method, which involved the spectral lines of neon (Ne). Several prominent peaks were identified and used for calibration. Figure 6.1a shows the detected peaks, while Figure 6.1b displays the resulting calibration function. For this calibration, the equation was $\lambda(p) = a \cdot \text{pix} + b$, where pix is the pixel number and λ is the wavelength. The coefficients were $a = 0.2303 \pm 0.0002$ and $b = 433.9 \pm 0.2$, calculated with a 95% confidence interval.

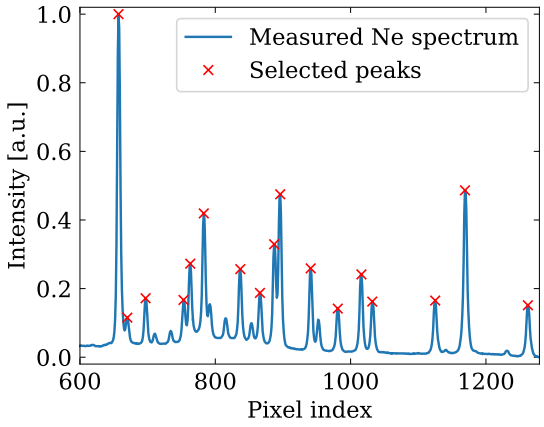

(a) Measured summed profile using Ne spectrum for calibration and selected peaks.

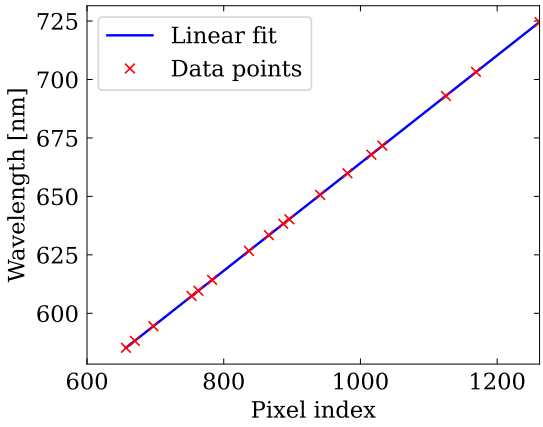

(b) Calibration line, using Ne known spectum. $\lambda = (0.2303 \pm 0.0002)\text{pix} + (433.9 \pm 0.2)$

Figure 6.1

However for the measurement with the zebrafish embryos, I used the calibration with the wavelength filters, beacuse I needed a rapid calibration.

After completing the alignment (see Chapter 4) and the calibration, I proceeded to perform measurements on multiple samples. As mentioned earlier, I captured images of zebrafish embryos, each approximately 3 mm in size. The samples were provided by the ELI Szeged facility, where radiobiological experiments on zebrafish embryos are conducted. The embryos were fixed in 4% paraformaldehyde (PFA) for 24 hours and stored in methanol at -20 °C.

Before the experiments, I washed them three times in PBS (1% salt solution) and kept them in PBS during examination. After the experiments, I placed them back into methanol to prolong the specimens shelf life.

I tested different sample holder configurations and obtained the best imaging results by placing small water droplets (0.1 ml) on top of the holder (Figure 6.2c). Up to 12 samples could be mounted simultaneously, after which I began the measurements. I ensured that all experimental conditions remained stable throughout the measurement process and I frequently checked the spectrum of the illumination source.

Since it was not possible to position each fish at exactly the same location (in the center of each holder slot), locating the sample during imaging was challenging because the camera captured only one spatial coordinate. The scanner moved along the x direction (see Figure 2.12a), while the samples were manually shifted in the y direction. To overcome this positioning difficulty, I installed a high-magnification camera directed toward the slit, which allowed me to view the image projected onto the slit and adjust the positioning accordingly also shown in Figure 6.2b. The image of a zebrafish on the slit is shown at Figure 6.2a. After each scan, I verified that the captured image was of acceptable quality. An Excel sheet was used to record and track all zebrafish samples that were imaged.

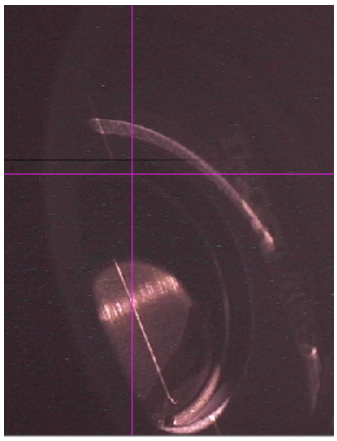

(a) Preview of the high-magnification monitoring camera, image of a fish on the slit.

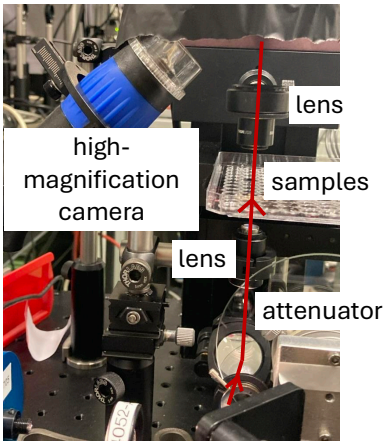

(b) High-magnification monitoring camera aligned toward the slit for positioning.

(c) Zebrafish embryos prepared for imaging.

Figure 6.2: Experimental setup and sample preparation for zebrafish embryo measurements.

Chapter 7

Hyperspectral Analysis of the Zebrafish Embryos

Following the optical design, construction of the hyperspectral microscope, characterization of its limitations, development of the software alongside the hardware, system setup, and data acquisition, the final step is the visualization and analysis of the measured data.

Analyzing this dataset is challenging due to significant noise. Zebrafish embryos are thin and largely see-through, so there is limited scattering as light passes through the tissue.

7.1 Data Visualization

Hyperspectral datasets can be visualized in several complementary ways to reveal spatial and spectral structure.

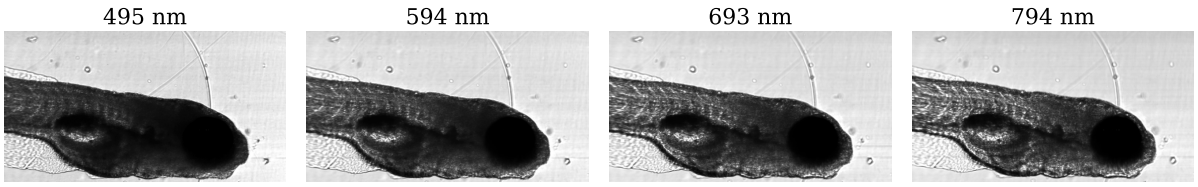

Figure 7.1: Raw hyperspectral images at different wavelengths under transmittive illumination.

One common approach is to display the images at different wavelengths side by side, as illustrated in Figure 7.1. A similar method involves stacking the images across wavelengths to visualize the hyperspectral data cube, as shown in Figure 7.2.

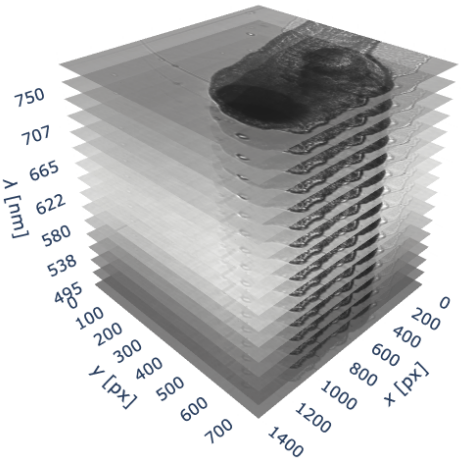

Figure 7.2: Stacked hyperspectral images forming a data cube representation using transmittive illumination (15 wavelengths are represented.)

Another widely used method is to select a specific pixel or a region of interest (ROI) and plot the corresponding spectral signature, as demonstrated in Figure 7.3. This approach provides detailed insight into the spectral properties of particular locations within the scene.

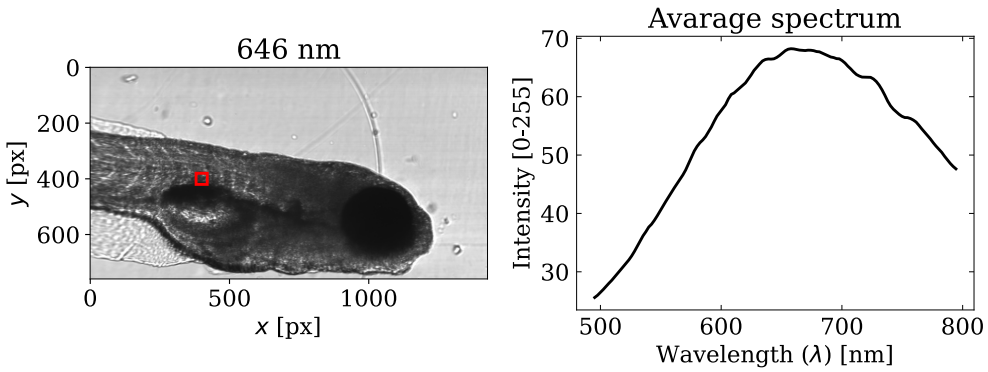

Figure 7.3: Spectrum of a selected region of interest (ROI) using transmittive illumination.

7.2 Data Analysis of Zebrafish Using Refractive Illumination

Under refractive illumination, some features of the embrio become more visible, like the pigments and the eye structure, however the fins remain largely undetected.

Measuring the spectral fingerprint of these specimens presents significant challenges due to their small size and high transparency. Consequently, light predominantly transmits through the tissue with minimal scattering. Conversely, in denser or darker regions, a substantial portion of the light is absorbed.

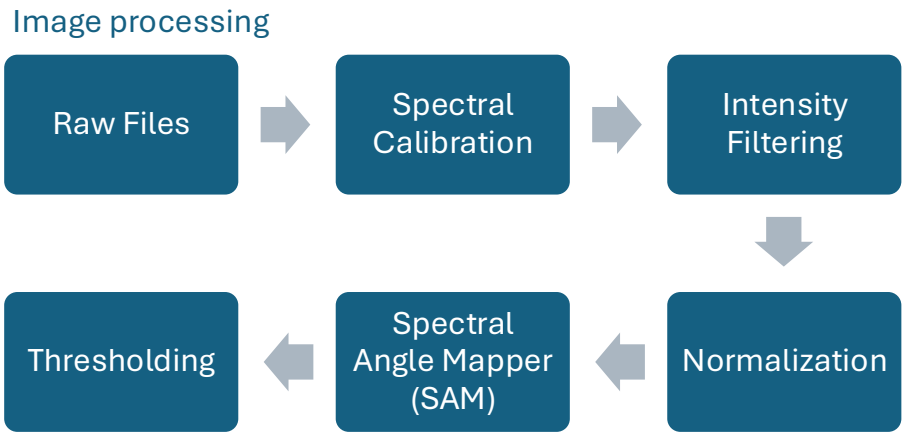

Figure 7.4: Steps of the image processing of the hyperspectral images.

Following data acquisition, several image processing steps were performed, as outlined in Figure 7.4. As previously mentioned, spectral calibration was conducted using a neon lamp to determine wavelength resolution. However, for routine measurements, I relied on interference filters (630 nm and 720 nm) to enable more effective adjustement of the device. By identifying the spectral positions of these two filters, I was able to calibrate the device effectively.

The capture settings included an exposure time of 0.07 sec, a gain of 5.0 dB, an image size of 1280x960 pixels, and a scanning velocity of 0.09 mm/sec.

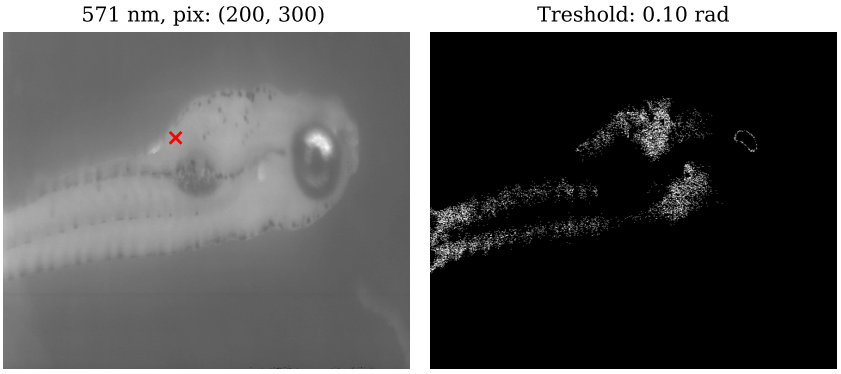

Figure 7.5: Grayscale image of the normalized data with reference point at 571 nm (left), and tresholded image (right).

After capturing the raw images and applying the calibration, I used an intensity mask to filter out pixels with exceptionally low intensities or high values caused by the blue peak of the white LED.

A white Plexiglas plate was used as the reference image during acquisition. The white reference spectrum was spatially averaged, and the measured data was normalized against this reference spectrum. ($A = A_{meas}/A_{white}$).

Earlier in this thesis, I introduced the Spectral Angle Mapper (SAM) method, which is well-suited for analyzing these hyperspectral images. For this analysis, I selected a reference point with a spectrum that corresponds to an n-dimensional vector. I then calculated the spectral angle between this reference vector and the spectral vectors of all other pixels in the image. By setting a specific angle threshold, I plotted the pixels that fell within this limit, as illustrated in Figure 7.5.

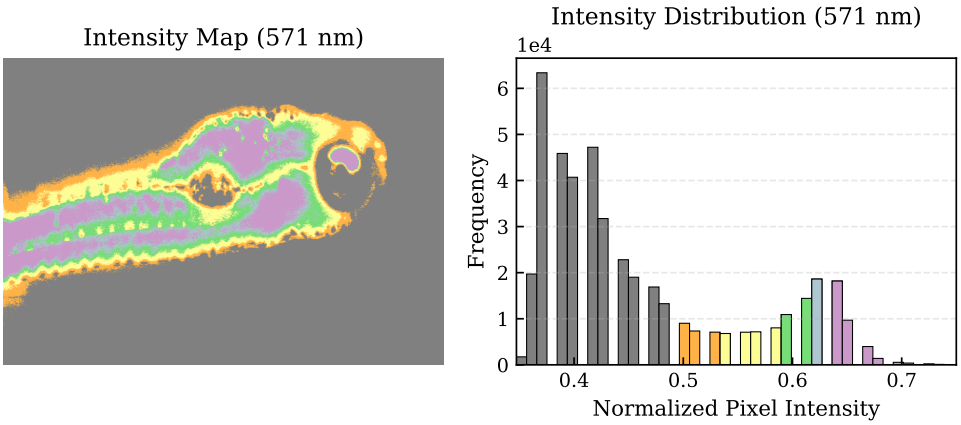

Figure 7.6: Inensity Map on the fish (left) based on the groups made on the histogram (right).

Theoretically, the SAM classification should be independent of intensity information, characterizing the image based purely on spectral differences. However, in practice, intensity variations still appear to influence the results.

To gain deeper visual insight, I generated a histogram (Figure 7.6) to evaluate the intensity distribution. The spectrum was quantized into five discrete groups, utilizing Otsu's method to separate the background. The resulting intensity map is also presented in Figure 7.6.

The histogram reveals that the normalized pixel intensity remains quite low within the interesting regions, indicating a low signal-to-noise ratio (SNR).

Fusing these analyses yields Figure 7.7. The background image maps the various intensity levels, while the red regions highlight the pixels that satisfy the SAM angle threshold. This analysis was performed using two different reference points: one targeting the contour (bone structures) and the other targeting the internal organs of the embryo.

As the figure demonstrates, spectrally similar regions (relative to the reference point) tend to cluster within regions of similar intensity. Ideally, if the system could fully resolve spectrally distinct organs, the intensity map would not perfectly correlate with the SAM classification.

This overlap indicates that the classification remains highly dependent on signal intensity, limiting its ability to separate structures based purely on spectral information.

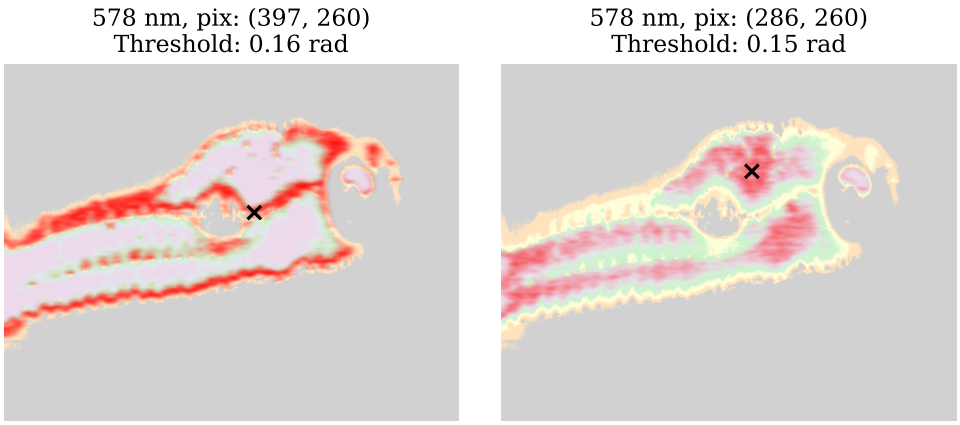

Figure 7.7: Intensity map, and thresholded angles from SAM (shown with red), using two different reference point.

While the instrument performs well with opaque, non-transparent materials such as colored paper (as demonstrated in Section 5.2), further development is required to effectively investigate and differentiate spectral regions within highly transparent zebrafish embryos.

7.3 Data Analysis of Zebrafish Using Transmissive Illumination

Using transmissive illumination, we can observe finer structures and more detail within the fish. This is because, as light passes through the sample, its intensity decreases, which increases contrast in small specimens. This is also the principle behind the use of transmissive illumination in microscopy.

I followed the same image-processing approach as in the case of reflective illumination. However, in this case, the data were normalized using the illumination spectrum instead of a white reference.

As shown in Figure 7.8, the acquired image was relatively dark, especially in the thicker regions of the fish. This also introduced a significant amount of noise.

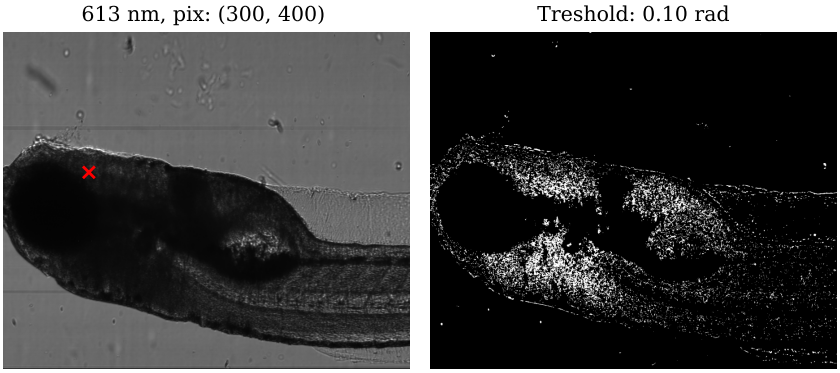

Figure 7.8: Grayscale image of the normalized data with reference point at 613 nm (left), and tresholded image (right) using transmissive illumination.

To reveal the finer structures of the fish, I again plotted the intensity distribution map, shown in Figure 7.9. The background is also separated, now within the high-intensity region.

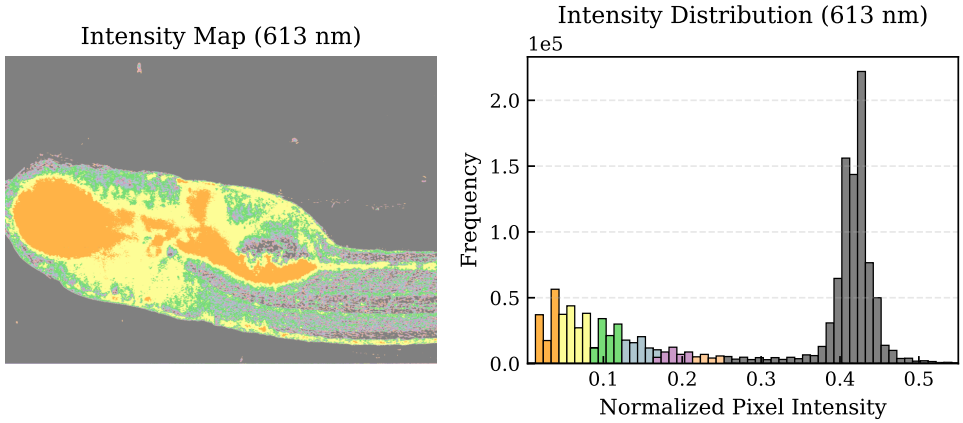

Figure 7.9: Inensity Map on the fish (left) based on the groups made on the histogram (right).

When thresholding the images using SAM to investigate whether this type of illumination would provide better intensity-independent results, I identified an interesting region, shown in Figure 7.10. This region corresponds to the location of the inner ear.

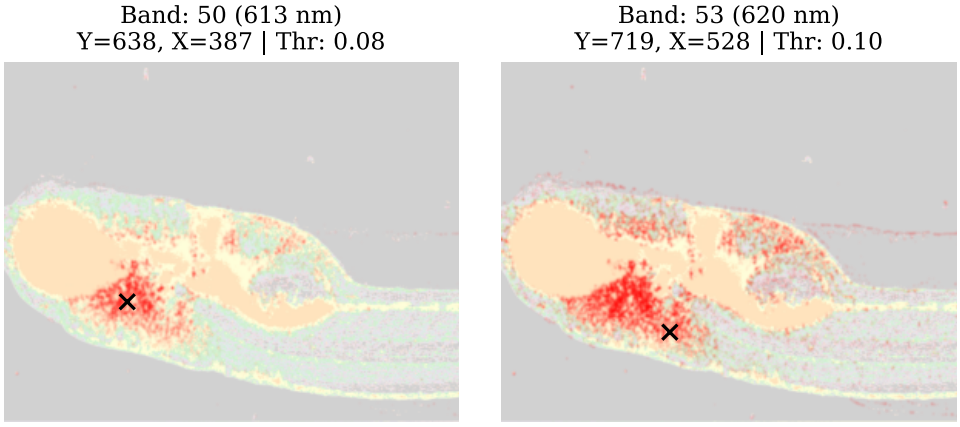

Figure 7.10: Intensity map, and thresholded angles from SAM (shown with red), using two different reference point.

This area forms a distinct region, and the same yellow coloration is not observed everywhere, which could suggest a degree of intensity independence. However, when other reference points were examined, this behavior was not consistently observed. In addition, these regions contain very low-intensity pixels (as shown in Figure 7.9), making the results less reliable. Ideally, one would expect to observe more distinct regions of this kind if the fish exhibited greater spectral variation.

Chapter 8

Conclusions

In this project, I designed and built a hyperspectral camera, which I later upgraded into a hyperspectral microscope. I designed the optical system, modelled it, and built it in the laboratory using a vertical configuration. For easy alignment and efficient measurements, I developed a program to control the servo motor and camera for image acquisition. I also created a graphical user interface for user-friendly operation. I made a simulation in Zemax, to assess the imaging properties of the setup.

In the optomechanical setup, I ensured proper alignment of all optical components along the correct degrees of freedom and then calibrated the measurement system. I performed spectral calibration using filters and a neon lamp. After careful alignment and calibration, the instrument achieved a magnification of 2.42, a wavelength resolution of 2.4 nm and a spatial resolution 8.3 μm in 300 nm wide spectral range in the visible spectrum, for example in $450 - 750$ nm range.

The system was first tested using colored reference samples, demonstrating that it could reliably detect and map different spectral signatures. It was then applied to identify the spectral fingerprints of zebrafish embryos. Two illumination methods were examined and compared: transmissive illumination and refractive illumination. Refractive illumination effectively highlighted surface pigments and dense structures such as the eye, while transmissive illumination provided better spatial contrast for observing internal organs.

Hyperspectral data was analyzed using the Spectral Angle Mapper (SAM) algorithm. In theory, SAM can identify spectral profiles independently of signal intensity. However, when applied to zebrafish embryos, several limitations became apparent. Due to the high transparency and absence of color of the specimens, measuring scattering is quite difficult. As a result, the measured spectral data were still heavily affected by intensity variations, making it difficult to separate true tissue-specific spectral information from background noise and structural differences.

By further improvement of the imaging setup, it would be possible to extend the wavelength range to near-IR and use advanced image processing methods. HSI has the potential in seeking for signatures of pathologies in ill versus control group of samples. When samples are screened in larger batches, the statistical methods based on machine learning can be used to assess subtle spectral patterns and classify pathological changes with higher sensitivity and robustness. Machine learning approaches such could help distinguish weak tissue-specific spectral signatures from noise and illumination-related artifacts. Combining hyperspectral imaging with automated segmentation and statistical evaluation may en-

able early detection of tissue degeneration or irradiation-induced changes, allowing subtle structural and biochemical alterations to be identified before they become visible through conventional imaging methods.

Overall, this work presents the development of a complete and functional hyperspectral microscopy platform, including optical design, hardware integration, and software development. The results demonstrate the inherent physical limitations of label-free hyperspectral imaging for highly transparent and minimally colored biological tissues.

By advancing the design and application of hyperspectral microscopy, this work contributes to the popularization and development of hyperspectral imaging as a promising technique in biomedical research.

Chapter 9

Acknowledgements

I would like to thank my supervisor, Václav Hanus, for his guidance throughout this work and for always being available to answer questions. I learned a great deal from him, from understanding optical phenomena, developing programming skills to working in the laboratory.

I would also like to thank Péter Dombi for his encouragement and the discussions that helped shape the direction of this project.

I am grateful to my colleagues at Wigner Research Centre for Physics for their thoughtful feedback and for creating a collaborative and friendly environment.

I appreciate the technical assistance from the ELI institute in Szeged and thank them for providing zebrafish embryos.

I would also like to thank Tadej Tomanic the visit to Ljubljana helped me gain better insight into different hyperspectral imaging devices and the local developments.

Bibliography

[1] Anuja Bhargava et al. “Hyperspectral imaging and its applications: A review”. In: *Heliyon* 10 (2024), e33208.

[2] Chao Chen, Yue Jiang, and Xiaoqing Zhu. “Research on Lettuce Canopy Image Processing Method Based on Hyperspectral Imaging Technology”. In: *Plants* 13 (2024), p. 3403.

[3] Ximing Zhou et al. “Polarized Hyperspectral Microscopic Imaging for Zebrafish”. In: *Proceedings of SPIE - The International Society for Optical Engineering* 12834 (2024).

[4] Håkon Høgset et al. “In vivo biomolecular imaging of zebrafish embryos using confocal Raman spectroscopy”. In: *Nature Communications* 11 (2020), p. 6172.

[5] Guolan Lu and Baowei Fei. “Medical hyperspectral imaging: A review”. In: *Journal of Biomedical Optics* 19 (2014), p. 010901.

[6] M. Joel and V.-D. Tuan. “Optical properties of tissue”. In: *Biomedical Photonics Handbook*. CRC Press, 2003. Chap. 2, pp. 1–76.

[7] Yue Wu et al. “Review on the Application of Hyperspectral Imaging Technology of the Exposed Cortex in Cerebral Surgery”. In: *Frontiers in Bioengineering and Biotechnology* 10 (2022), p. 906728.

[8] K. Howe et al. “The zebrafish reference genome sequence and its relationship to the human genome”. In: *Nature* 496 (2013), pp. 498–503.

[9] C. Hoi et al. “Zebrafish as an animal model for biomedical research”. In: *Experimental and Molecular Medicine* 53 (2021), pp. 310–317.

[10] Szegedi Tudományegyetem. *Gyakorlati jegyzet Állatkísérletek elmélete és gyakorlata*. 2025.

[11] E. R. et al. Szabó. “Radiobiology Investigation on low-intensity neutron beam using zebrafish embryo model”. In: *Radiotherapy and Oncology* 206 (2025), S3960.

[12] Ting Xu et al. “Leveraging zebrafish models for advancing radiobiology: Mechanisms, applications, and future prospects in radiation exposure research”. In: *Environmental Research* 266 (2025), p. 120504.

[13] Rebecca von Hellfeld et al. “Adverse effects in the fish embryo acute toxicity (FET) test: A catalogue of unspecific morphological changes versus more specific effects in zebrafish (Danio rerio) embryos”. In: *Environmental Sciences Europe* 32 (2020), p. 122.

[14] Sujata Chakravarty et al. “Hyperspectral Image Classification using Spectral Angle Mapper”. In: *2021 IEEE International Women in Engineering (WIE) Conference on Electrical and Computer Engineering (WIECON-ECE)*. 2021, pp. 246–249.

[15] Ali Zahavi et al. “Influence of illumination sources on hyperspectral imaging”. In: *2019 IEEE International Conference on Imaging Systems and Techniques (IST)*. 2019, pp. 1–6.